



Contents lists available at SciVerse ScienceDirect

## Journal of Sound and Vibration

journal homepage: [www.elsevier.com/locate/jsv](http://www.elsevier.com/locate/jsv)

# Performances of the Partition of Unity Finite Element Method for the analysis of two-dimensional interior sound fields with absorbing materials

J.-D. Chazot<sup>a</sup>, B. Nennig<sup>b</sup>, E. Perrey-Debain<sup>a,\*</sup>

<sup>a</sup> Laboratoire Roberval, Université de Technologie de Compiègne, 60205, Compiègne BP 20529, France

<sup>b</sup> Laboratoire d'Ingénierie des Systèmes Mécaniques et des Matériaux, Supméca (LISMA), SUPMECA, 3 rue Fernand Hainaut, 93407 St Ouen Cedex, France

## ARTICLE INFO

### Article history:

Accepted 24 June 2012

Handling Editor: J. Astley

Available online 8 July 2012

## ABSTRACT

The paper deals with the numerical simulation of the acoustic field in two-dimensional cavities in which absorbing materials are present. Though Finite Element Method (FEM) could be employed for this purpose, the discretization level required for achieving reasonable accuracy renders the method impractical in the mid-frequency range. To alleviate this limitation, the Partition of Unity Finite Element Method (PUFEM) using plane wave functions has been shown to be very effective for solving short wave Helmholtz problems. In the present work, the method is extended to the computation of the pressure wave field within the absorbing media which is modeled as a bulk-reacting material characterized by a complex-valued and frequency dependent mean density and dynamic compressibility. Lagrange multipliers are used to enforce the transmission conditions at the air–material interface. Performances of the PUFEM are compared with a standard FEM in several examples of practical interests. It is shown that the technique is a good candidate for solving noise control problems at high frequency.

© 2012 Elsevier Ltd. All rights reserved.

## 1. Introduction

Porous absorbers are now commonly used as passive noise control solutions in order to reduce the sound pressure field in enclosed cavities. The type of applications ranges from room acoustics predictions, sound proofing of aircrafts or cars' passenger compartments to muffler designs in HVAC systems. In practice, an accurate prediction of the acoustic performances is obtained via computational methods such as the very popular Finite Element Method (FEM) or the Boundary Element Method (BEM) [1]. However, these methods are known to be extremely demanding computationally when the frequency increases, or when the dimensions of the domain are too large, and are thus limited to 'low' frequency applications. This limitation stems from the typical rule-of-thumb that around 10 nodes per wavelength are required in order to capture the oscillatory behavior of the wave. To make the matter worst, for a certain class of absorbent materials such as polymer foams, the solid structure has a finite stiffness. In this case, Biot's theory describing the propagation of elastic and pressure waves in the poroelastic material must be used [2]. As opposed to air waves Biot's waves are damped and propagate much slower. Again, this limits the analysis to reduced-size configurations [3].

In order to tackle medium to high frequency problems, the last decade has seen the emergence of new approaches in which the solution to the problem is expanded in the basis of oscillatory wave functions [4]. Though this is not the place

\* Corresponding author. Tel.: +33 44 23 46 41.

E-mail address: [emmanuel.perrey-debain@utc.fr](mailto:emmanuel.perrey-debain@utc.fr) (E. Perrey-Debain).

for a complete survey, we can cite the Partition of Unity Finite Element Method (PUFEM) [5], the Ultra-Weak formulation [6,7], the Discontinuous Galerkin Method [8], the Wave Boundary Element Method [9], the Wave Based Method [10,11] and the Variational Theory of Complex Rays [12]. All these methods have in common that they offer a drastic reduction in degrees of freedom as compared with conventional discretization schemes. Among all these techniques, the PUFEM has the advantage to be very similar to the FEM and its numerical implementation can be easily adapted to any FEM mesh. Applications of the PUFEM using plane waves and/or Bessel functions for the computation of acoustic and elastic waves can be found in recent papers [13–16].

One direction of particular interest to us is to extend the PUFEM for the numerical computation of the sound field in cavities filled with air in contact with porous absorbing materials. In the present work, the computational model is simplified by assuming that the material reacts like an equivalent fluid. Although this restricts the analysis to a certain class of absorbing materials, this assumption is widely used, especially at high frequencies where the solid phase response is not predominant (see a detailed discussion in Chapter 6 in [2]). Furthermore, this work must be considered as a starting point for further development of the PUFEM for tackling the more general problem of Biot’s waves propagation in poroelastic materials.

The present paper is organized as follows. The PUFEM formulation is presented in Section 2. In each domain (air and porous material) the acoustic pressure is discretized using a set of plane waves with real or complex wavenumbers whereas the continuity of pressure and velocity at the air–porous interface is enforced by the use of Lagrange multipliers. In Section 3, the performances of the method, measured in terms of data reduction, are assessed against a one-dimensional problem for which an analytical solution is available. In the last section, the interest of the method is illustrated on various examples of practical interest such as the analysis of interior sound fields in a car’s passenger compartment.

## 2. Formulation

### 2.1. Problem statement

The general interior problem under consideration is illustrated in Fig. 1. It consists of a bounded two-dimensional domain  $V = V_a \cup V_p$  where  $V_a$  is a air-filled cavity with density  $\rho_a$  and sound speed  $c_a$  and the domain  $V_p$  is filled with a porous absorber. For a brief nomenclature, all quantities associated with the air cavity are referred by the subscript  $a$  whereas the porous domain is denoted by the subscript  $p$ . In the frequency domain (the time dependence  $e^{-i\omega t}$  is assumed), the governing equation for the acoustic pressure in the air is the classical Helmholtz equation

$$\Delta p_a + k_a^2 p_a = 0 \quad \text{in } V_a, \tag{1}$$

where  $k_a = \omega/c_a$  is the wavenumber and  $\omega$  is the harmonic frequency. The propagation model for porous absorbers with a rigid skeleton is given by the well-known equivalent fluid approach. The porous absorber is modeled as a fluid medium characterized by a complex wavenumber  $k_p$  and a complex density  $\rho_p$  [2]. The pressure in the porous material satisfies

$$\Delta p_p + k_p^2 p_p = 0 \quad \text{in } V_p. \tag{2}$$

Here,  $k_p = \omega(\rho_p/K_p)^{1/2}$  and quantities such as the density and the dynamic fluid compressibility  $K_p$  are calculated from the Johnson–Champoux–Allard’s model [2] (see the Appendix).

The coupling conditions at the air–porous interface (here denoted  $S_{ca}$  and  $S_{cp}$ ) are obtained by imposing the continuity of pressure and normal velocity across the interface:

$$\frac{\phi}{\rho_p} \frac{\partial p_p}{\partial n_p} = - \frac{1}{\rho_a} \frac{\partial p_a}{\partial n_a}, \tag{3}$$

$$p_p = p_a, \tag{4}$$

where  $n_p$  and  $n_a$  are the outward normals of each domain so  $n_p = -n_a$  and  $\phi$  is the porosity. On the other part of the boundary of the air cavity ( $S'_a$ ), a prescribed normal velocity  $v_a$  is imposed:

$$\frac{\partial p_a}{\partial n_a} = i\rho_a \omega v_a \quad \text{in } S'_a, \tag{5}$$

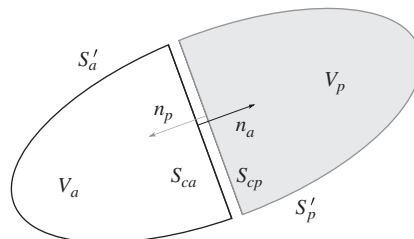


Fig. 1. Studied configuration.

whereas the porous absorber is assumed to be in contact with rigid walls, that is

$$\frac{\partial p_p}{\partial n_p} = 0 \quad \text{in } S_p'. \quad (6)$$

## 2.2. Variational formulation

A standard weighted residual scheme is applied to the Helmholtz equation, so the inner product

$$\int_{V_\alpha} (\Delta p_\alpha + k_\alpha^2 p_\alpha) \delta p_\alpha \, dV, \quad \alpha = a \text{ or } p, \quad (7)$$

where  $\delta p_\alpha$  is a properly chosen weighting function, gives the governing integral equation for the problem. After integration by parts, the problem in both domains ( $\alpha = a, p$ ) is formulated in a weak form as

$$\int_{V_\alpha} (\nabla p_\alpha \cdot \nabla \delta p_\alpha - k_\alpha^2 p_\alpha \delta p_\alpha) \, dV - \int_{\partial V_\alpha} \frac{\partial p_\alpha}{\partial n_\alpha} \delta p_\alpha \, dS = 0. \quad (8)$$

By following the steps of the work published in Ref. [16], we now introduce  $\Lambda$ , the Lagrange multiplier defined as the normal derivative of the acoustic pressure at the air–porous interface. The variational formulation for the air cavity writes

$$\int_{V_a} (\nabla p_a \cdot \nabla \delta p_a - k_a^2 p_a \delta p_a) \, dV - \int_{S_{ca}} \Lambda \delta p_a \, dS = i \rho_a \omega \int_{S_a} v_a \delta p_p \, dS. \quad (9)$$

And similarly,

$$\frac{\phi \rho_a}{\rho_p} \int_{V_p} (\nabla p_p \cdot \nabla \delta p_p - k_p^2 p_p \delta p_p) \, dV + \int_{S_{cp}} \Lambda \delta p_p \, dS = 0 \quad (10)$$

for the porous domain. Applying standard Lagrange multiplier techniques, the continuity of pressure across the air–porous interface is weakly enforced as

$$\int_{S_c} (p_p - p_a) \delta \Lambda \, dS = 0, \quad (11)$$

where  $\delta \Lambda$  is an appropriate weight function and  $S_c = S_{ca} = S_{cp}$  denotes the air–porous common interface. We can note that the formulation (10) was deliberately multiplied by the factor  $\phi \rho_a / \rho_p$  for symmetry reasons as shown in the next section.

## 2.3. Plane wave finite elements and integration

Let the domain  $V$  be partitioned into  $L$  non-overlapping subdomains  $V^{(l)}$  where  $l$  ranges from 1 to  $L$ . Each sub-domain, or finite element in the engineering terminology, is defined via the geometric mapping  $\mathbf{r} = \mathbf{r}^{(l)}(\xi, \eta)$  between the real space and the local system of triangular type

$$\mathcal{T} = \{\xi \geq 0, \eta \geq 0, \xi + \eta \leq 1\}.$$

The key ingredient of the PUFEM relies on the enrichment of the conventional finite element approximation by including solutions of the homogeneous partial differential equation. In the Helmholtz case plane waves, circular waves (Bessel functions) and wave bands are commonly used [5,15–17]. In this work, plane waves are chosen for their simplicity. In each sub-domain  $V^{(l)}$ , the acoustic pressure is expanded as

$$p_\alpha(\mathbf{r}) = \sum_{j=1}^3 \sum_{q=1}^{Q_{\alpha,j}} N_j^3(\xi, \eta) \exp(ik_\alpha \mathbf{d}_{\alpha,jq} \cdot (\mathbf{r} - \mathbf{r}_j^{(l)})) A_{\alpha,jq}^{(l)}, \quad (12)$$

where the plane waves amplitudes  $A_{\alpha,jq}^{(l)}$  are unknown coefficients and functions  $N_j^3$  are the classical linear shape functions on triangular elements. Points  $\mathbf{r}_j^{(l)}$  are the three nodes associated with element  $V^{(l)}$ . Their presence in (12) ensures that the nodal values are recovered simply as

$$p_\alpha(\mathbf{r}_j^{(l)}) = \sum_{q=1}^{Q_{\alpha,j}} A_{\alpha,jq}^{(l)} \quad (13)$$

and that plane waves amplitudes of the porous domain are not spoiled by the complex character of the wavenumber. This fact is discussed further in the next section. The directions, attached to node  $j$ , are chosen to be evenly distributed over the unit circle, that is

$$\mathbf{d}_{\alpha,jq} = (\cos(\theta_q), \sin(\theta_q)) \quad \text{where } \theta_q = \frac{2\pi q}{Q_{\alpha,j}}, \quad q = 1, \dots, Q_{\alpha,j}. \quad (14)$$

The number of plane waves attached to each node  $j = 1, 2, 3$  must be dependent on the frequency and the element size. Although there is no rigorous theory in this matter as this number might also depend on the studied configuration, there is a common acceptance that the following criteria should provide a good estimate [18]:

$$Q_{a,j} = \text{round}[k_a h + C(k_a h)^{1/3}]. \tag{15}$$

Here,  $h$  is taken as the largest element edge length connected to node  $j$  within the acoustic domain and the constant  $C$  is usually chosen to lie in the interval  $C \in [2, 20]$ . This coefficient can be adjusted depending on the configuration and the expected accuracy. Note that Eq. (15) is restricted to two-dimensional domains. For the porous domain, the same criteria is applied with the real part of the wavenumber since it corresponds to the oscillating part of the solution:

$$Q_{p,j} = \text{round}[\text{Re}(k_p)h + C(\text{Re}(k_p)h)^{1/3}]. \tag{16}$$

Similarly,  $h$  is taken as the largest element edge length connected to node  $j$  within the porous domain.

In the present work, the finite element geometries are defined using standard quadratic shape functions on triangular elements:

$$\mathbf{r}^{(l)}(\xi, \eta) = \sum_{j=1}^6 N_j^6(\xi, \eta) \mathbf{r}_j^{(l)} \tag{17}$$

as this description is integrated in most softwares (here the finite element mesh generator `Gmsh` is used [19]). In Eq. (17) extra nodes  $\mathbf{r}_j^{(l)}$  for  $j = 4, 5, 6$  correspond to the mid-node of the edges as shown in Fig. 2. On both sides of the air–porous interface, meshes are designed to be compatible. This choice is made for practical reasons as it considerably eases the numerical implementation of the method. At the matching interface, the Lagrange multiplier is expanded using real plane waves with the highest oscillations (i.e.  $\text{Re}(k_p)$ ), that is

$$\Lambda(\mathbf{r}) = \sum_{j=1}^2 \sum_{q=1}^{Q_{p,j}} N_j^2(\xi) \exp(i\text{Re}(k_p) \mathbf{d}_{p,jq} \cdot (\mathbf{r} - \mathbf{r}_j^{(l)})) \lambda_{jq}^{(l)}, \tag{18}$$

where amplitudes  $\lambda_{jq}^{(l)}$  are unknown coefficients, linear functions  $N_j^2$  are simply the restriction of the shape functions  $N_j^3$  on the boundary line  $S_c$  and the superscript  $(l)$  refers to the adjacent element  $V^{(l)}$  belonging to the porous domain. Finally, the element matrices are formed using a Galerkin scheme: the weight functions  $\delta p_\alpha$  ( $\alpha = a, p$ ) and  $\delta \Lambda$  are chosen from the plane wave basis (12) and (18). This is the so-called unconjugated formulation [14] which renders the algebraic system symmetric with the following form:

$$\begin{pmatrix} \mathbf{K}_a & 0 & -\mathbf{C}_a \\ 0 & \mathbf{K}_p & \mathbf{C}_p \\ -\mathbf{C}_a^T & \mathbf{C}_p^T & 0 \end{pmatrix} \begin{pmatrix} \mathbf{A}_a \\ \mathbf{A}_p \\ \Lambda \end{pmatrix} = i\rho_a \omega \begin{pmatrix} \mathbf{V}_a \\ 0 \\ 0 \end{pmatrix}. \tag{19}$$

Here  $\mathbf{K}_\alpha$  are the plane wave finite element matrices for the Helmholtz problem,  $\mathbf{C}_\alpha$  the coupling matrices and vectors  $\mathbf{A}_\alpha$  ( $\alpha = a, p$ ) and  $\Lambda$  contain the plane wave amplitudes in (12) and (18). As plane wave finite elements may span many wavelengths the computation of the element matrices requires the integration of highly oscillating functions, especially in the porous domain where the real part of the wavenumber can be much larger than the acoustic one. This procedure may prove costly from a numerical point of view so some precautions must be taken in order to avoid penalizing and time-consuming calculations. Recently, progress has been made to perform the integration analytically using various mathematical techniques [20–22]. Unfortunately, these developments cannot be applied to curved elements. In passing, we think that there is scope for further research in this direction. In the present work, the integration is performed using the adaptive Gauss quadrature algorithm `gauleg` from Numerical Recipes [23]. In each sub-domain a set of Gauss points and weights are stored. All geometric information independent of the plane wave basis such as the value of shape functions  $N_j^3$  and their derivatives at the quadrature points are also precomputed and stored.

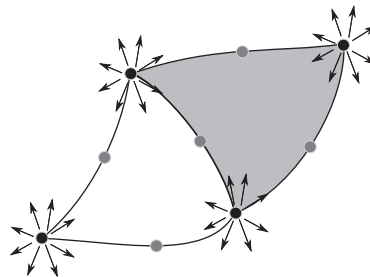


Fig. 2. Plane wave finite element with quadratic geometry and matching mesh.

### 3. Study of the PUFEM performances with absorbing materials

Since the emergence of plane waves-based computational methods in the mid-1990s, the method has received some attention from the applied mathematicians community. Theoretical analysis concerning convergence with real plane waves can be found, for instance in [5,6,24,25]. Although, it would be interesting to extend the study to plane waves with complex wavenumbers, such an analysis is clearly beyond the scope of this paper. The aim of this section is to highlight the performances of the method from a practical point of view. In this regard, an interesting point is to evaluate the average number of degrees of freedom per wavelength necessary to ensure a good approximation of the solution. Due to the disparity in speed of sound between the air and the porous media, it is convenient to simplify the analysis by taking an artificial value for the porous wavenumber as  $k_p = k_a(1 + \chi i)$  where  $\chi$  is defined as the ratio between the imaginary and the real part of  $k_p$ . With this definition, the wavelength  $\lambda = 2\pi/k_a$  is identical in both domains so we can define the number of wavelengths spanning over a characteristic element length  $h_{\text{mesh}}$  of the finite element mesh as

$$\beta = \frac{h_{\text{mesh}}}{\lambda}. \tag{20}$$

By calling  $N_{\text{dof}}$  the total number of degrees of freedom, the average discretization level  $n_\lambda$  defined as the number of variables needed to capture a single wavelength is evaluated via

$$n_\lambda = \lambda \sqrt{\frac{N_{\text{dof}}}{\text{area}(V)}}. \tag{21}$$

For instance, using conventional finite element discretization, it is widely accepted that numerical solutions are expected to be of acceptable accuracy if around  $n_\lambda = 10$  nodes per wavelength are used and this corresponds to  $\beta = 0.1$  or 0.2 depending on the order of approximation (i.e. linear or quadratic).

Now, from the relation (15), the average discretization level associated with the PUFEM can be anticipated. Indeed, in the particular and ideal case of a regular triangular mesh of infinite extent as shown in Fig. 3, it is easy to see that

$$n_\lambda^{\text{ideal}} = \frac{\lambda}{a} \sqrt{Q} = \frac{1}{\beta} \sqrt{4\pi\beta + 2C(2\pi\beta)^{1/3}}, \tag{22}$$

where the number of plane waves directions  $Q$  attached to each node is calculated via (15) and  $h_{\text{mesh}} = a\sqrt{2}$ . The performance of the method for this ideal scenario is illustrated in Fig. 4 for three typical values:  $C=2, 10$  and  $20$  (dotted lines). Clearly, for a fixed mesh the gain in terms of data reduction (i.e. low  $n_\lambda^{\text{ideal}}$ ) grows as the frequency increases. To be more precise, a substantial gain is observed if the element size spans over few wavelengths: above 5 wavelengths, a discretization level of 3 degrees of freedom per wavelength is more than sufficient to ensure a converged solution, this fact was confirmed numerically in [16] for the PUFEM, and also for the Wave Boundary Element Method [26]. We can also notice from (22) that

$$\lim_{\beta \rightarrow \infty} n_\lambda^{\text{ideal}} = 0, \tag{23}$$

which means that very high frequency numerical solutions can be obtained with almost 0 degree of freedom per wavelength! This somewhat surprising fact is simply reflected in the formula (15) indicating that the number of variables needed to simulate approximately  $\beta^2$  wavelengths in the two-dimensional wave field behaves almost linearly with respect to  $\beta$ . Finally, an elementary sensitive analysis shows that

$$\Delta n_\lambda^{\text{ideal}} = \frac{\partial n_\lambda^{\text{ideal}}}{\partial C} \Delta C \quad \text{where} \quad \frac{\partial n_\lambda^{\text{ideal}}}{\partial C} = \frac{(2\pi)^{1/3}}{\beta^{5/3} n_\lambda^{\text{ideal}}}. \tag{24}$$

Thus, for sufficiently large  $\beta$  the value of  $C$  has a marginal impact on the efficiency of the method.

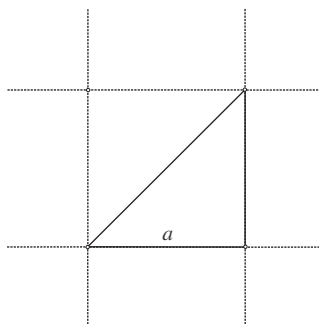


Fig. 3. Ideal mesh of infinite extent.

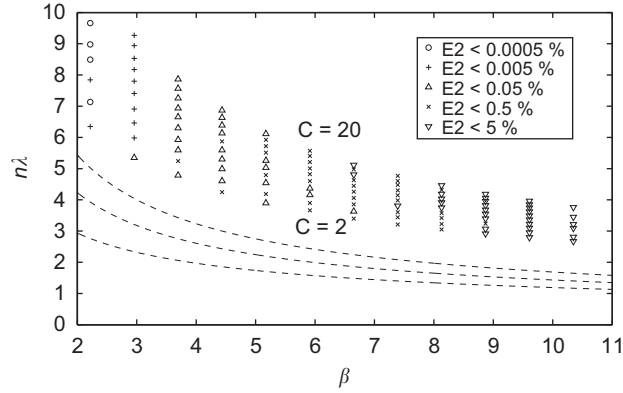


Fig. 4. Performances of the PUFEM: ideal scenario (dotted lines) and the standing wave tube test with  $\chi = 0.1$  (symbols). The relative error  $E_2$  stands for the quadratic error.

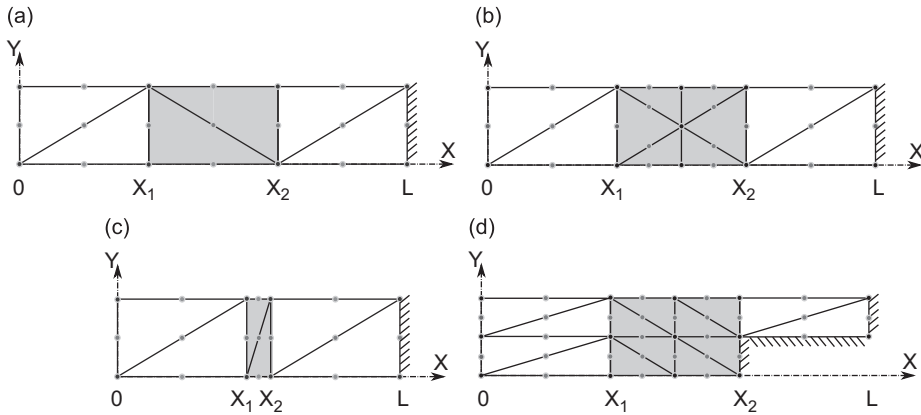


Fig. 5. The standing wave tube test (the gray color refers to the porous material): regular subdivision (a), regular subdivision with smaller elements in the porous domain (b), small porous layer (c), with variable backing (d).

Now, in order to verify this numerically, the first series of tests concerns that of a standing wave tube which geometry is illustrated in Fig. 5(a). The triangular mesh used in our calculation is also shown. The tube of length  $L = 0.15$  m is divided into three regions of equal length with  $x_1 = L/3$  and  $x_2 = 2L/3$ . The first region contains the incident and reflected wave and a normal velocity is imposed at the left wall. The second area (in gray) is the porous absorber. The last region is an air gap terminated by a rigid wall. This simple test case is chosen as one-dimensional analytical solutions are easily obtained and it corresponds to configurations of practical interest [11]. For this configuration, the characteristic length of the mesh is the longest edge, that is  $h_{\text{mesh}} = \sqrt{0.05^2 + 0.03^2} \approx 0.06$  m where the width of the tube is 0.03 m.

Through intensive calculations, the dependence between the discretization level  $n_x$ , the element length (in  $\beta$ ) and the coefficient  $C$  is conveniently reported in Fig. 4. Here, all symbols correspond to numerical results with less than five percent deviation compared with the analytical solution; the wavenumber in the porous domain is arbitrarily chosen to be  $k_p = k_a(1 + 0.1i)$  and we took  $\phi = 1$  and  $\rho_a = \rho_p$ . As the exact solution can be expressed as the sum of two horizontal plane waves propagating in opposite directions, all calculations were performed without the horizontal directions in order to ensure that the exact solution is not included in the plane wave basis. To be more precise, we take

$$\theta_q = \frac{2\pi(q+1/2)}{Q_{x,j}} \tag{25}$$

in (14) where the number of waves directions  $Q_{x,j}$  is an even number.

The curves show trends that are comparable with the ideal ones though the gain in terms of data reduction is not as good. This difference is simply due to the finiteness of the domain (i.e. the contribution of the plane wave basis associated with nodes on the boundary is restricted to the interior domain), the relatively small number of elements and the additional number of degrees of freedom (the Lagrange multiplier) at the air–porous interfaces. When the number of elements is sufficiently large, performances are found to be closer to the ideal curves. This will be illustrated through numerical examples in the next section.

For elements of small size, i.e.  $\beta$  small, the sensitivity analysis shows that the coefficient  $C$  has an impact on the efficiency of the method. In this regard, we can note that results of reasonable accuracy ( $< 5\%$ ) can still be

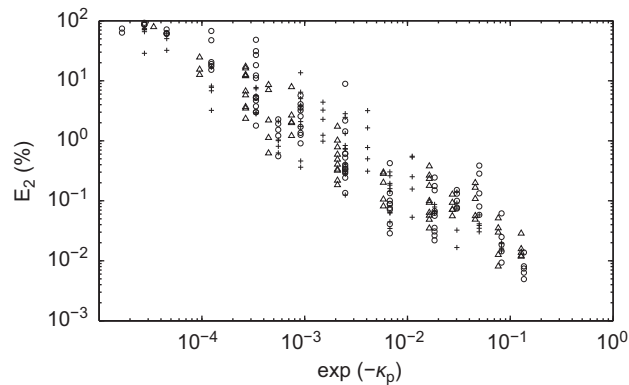


**Fig. 6.** Influence of the parameter  $\kappa_p$  on the quality of the solution. Symbols refer to the mesh used in the calculation: mesh (a) (cross), mesh (b) (triangle), and mesh (c) (circle).

achieved using the low value  $C=2$ . Depending on the complexity of the problem, this coefficient may have to be chosen larger as shown later.

In the high frequency regime, i.e.  $\beta > 10$ , larger errors are likely to occur. This observation which is absent in the undamped acoustic case is a consequence of the damping properties of the porous absorber. A closer analysis reveals that the degradation of the plane wave approximation is closely related to the magnitude of

$$\kappa_p = \text{Im}(k_p)h_{\max}, \quad (26)$$

where  $h_{\max}$  is the largest element edge within the porous domain. The reasons for this can be explained by the cumulative impact of two factors. The first one stems from the ill-conditioned nature of the algebraic system (19) which is inherent in all plane-waves based computational methods. The second one is the loss of accuracy due to round-off errors in the recombination of plane waves in (12) due to the large disparity in magnitudes between coefficients in the summation and, in the worst case, these coefficients range from  $\exp(-\kappa_p)$  to  $\exp(\kappa_p)$ . It is interesting to note that this numerical problem is also encountered with Mode Matching techniques when strongly evanescent modes needed to capture the wave field in the vicinity of a geometric singularity give rise to numerical discrepancies due to round-off errors [27]. The previous analysis is confirmed and illustrated in Fig. 6 where estimations of the quadratic errors ( $E_2$ ) are plotted against the quantity  $\exp(-\kappa_p)$  for three different meshes of Fig. 5 (denoted by appropriate symbols) and for a large range of numerical tests. Here, we took different values for  $k_a$  and  $C$  whereas the ratio  $\chi$  is chosen in the interval  $[0.1, 0.4]$ . Results, conveniently plotted on a logarithmic scale, show similar trend irrespective of the mesh structure. They indicate that below a certain threshold (say  $\exp(-\kappa_p) < 10^{-3}$  or  $\exp(-\kappa_p) < 10^{-2}$  depending on the expected accuracy), round-off errors are likely to be too penalizing giving rise to corrupted results. It should be noticed that the errors are calculated in the region of interest (i.e.  $0 < x < x_1$ ) and errors in the silent zone (i.e.  $x_2 < x < L$ ) are usually higher (by an order of magnitude at most) as the amplitude of the acoustic pressure in this region is considerably smaller. The fact that  $\kappa_p$  should not exceed a certain value restricts the finite element mesh size of the porous domain and thus appears to be a limiting factor. This is not necessarily a major issue as the numerical examples presented in the next section will show.

#### 4. Numerical examples

In this section, the efficiency of the method is discussed and illustrated on various examples of practical interest. The acoustic properties of the sound absorbing porous materials are taken from Refs. [28,29] and reported in the Appendix. The first example concerns that of the standing wave tube of Fig. 5(a). The graph of the acoustic pressure (in dB) with respect to the horizontal axis is shown in Figs. 7 and 8 for materials A and B. These results correspond to a high frequency calculation with  $f=20\,000$  Hz and each element contains about 3–4 wavelengths. The comparison with the analytical curve, in solid line, shows good agreements with about one percent relative error. In these examples, results are computed by taking  $C=5$  and convergence was reached with only  $C=2$ . The curve of Fig. 7 shows a sound transmission loss of about 50 dB between the incident and the silent zone. In this case, the parameter  $\kappa_p$  associated with the mesh of Fig. 5(a) is relatively high as we have  $\exp(-\kappa_p) \approx 0.0005$ .

The second test concerns that of the standing wave tube with variable backing as shown in Fig. 5(d). This example illustrates the performance of the PUFEM for tackling corner singularities. Fig. 9 shows the sound pressure level in the tube at 20 000 Hz when no material is present. We can observe that the scattering of waves by the corner generates the second transverse mode in the tube. This mode does not appear when a porous absorber is placed in the tube, as shown in Fig. 10. In both examples, results are computed using  $C=5$ . This was sufficient to ensure numerical solutions of engineering accuracy. In this regard, the accuracy could be greatly enhanced by using appropriate fractional Fourier–Bessel functions as shown in [30].

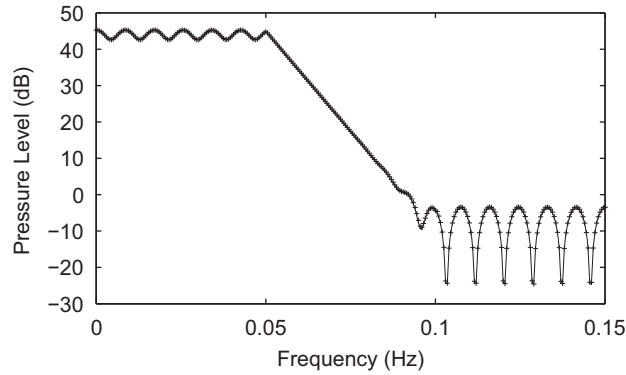


Fig. 7. The standing wave tube test with material A,  $f=20\ 000$  Hz: analytical solution (solid line) and PUFEM results (cross symbol).

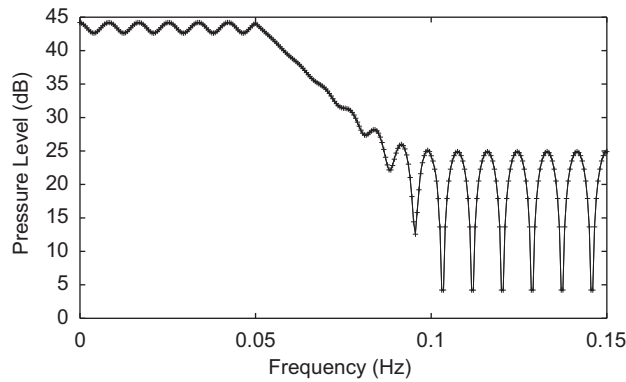


Fig. 8. The standing wave tube test with material B,  $f=20\ 000$  Hz: analytical solution (solid line) and PUFEM results (cross symbol).

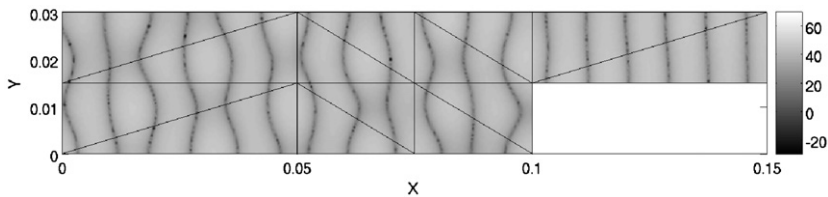


Fig. 9. The standing wave tube test with no material,  $f=20\ 000$  Hz.

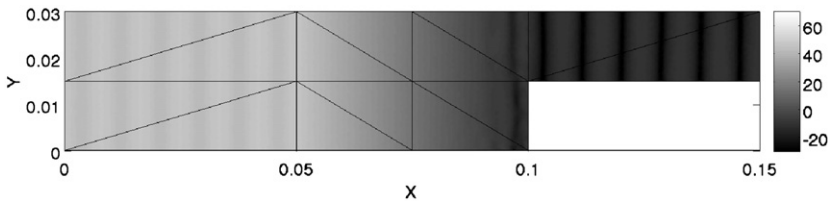
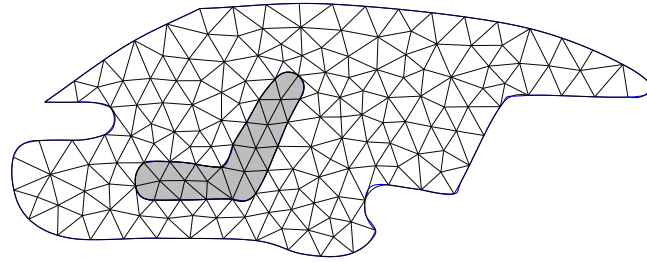
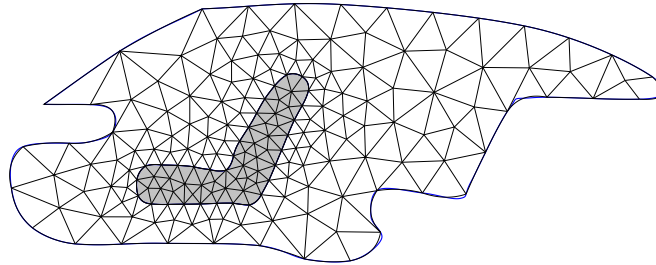


Fig. 10. The standing wave tube test with material C placed on variable backing,  $f=20\ 000$  Hz.

In the last example, the PUFEM is applied to the numerical estimation of the sound field in a 2D interior car cavity. The geometry and the PUFEM meshes used in our calculation are shown in Figs. 11 and 12. The sound field is generated by imposing an arbitrary normal velocity at the front windscreen (we simply put  $\partial p_a / \partial n_a = 1$ ). The car seat, in gray color, is filled with a porous material. In Fig. 13 are shown the distribution of sound in the car cavity at a frequency of 5000 Hz. The PUFEM results were computed using the coarse mesh 1 with material D and convergence was reached using  $C=15$ . The total number of degrees of freedom, including the Lagrange multipliers, is 8030. A rough estimate of the performance of the method can be obtained by calculating the average discretization level in (21). By taking  $c_a = 342$  m/s and  $\text{area}(V) = 2.76$  m<sup>2</sup>, we find that  $n_\lambda \approx 3.7$ . Note this estimate is overestimated as it is based solely on the acoustic wavelength. For the sake of comparison, the same calculation was performed with a standard FEM with quadratic



**Fig. 11.** Model of two-dimensional car interior cavity: coarse mesh 1. (For interpretation of the references to color in this figure caption, the reader is referred to the web version of this article.)



**Fig. 12.** Model of two-dimensional car interior cavity: coarse mesh 2.

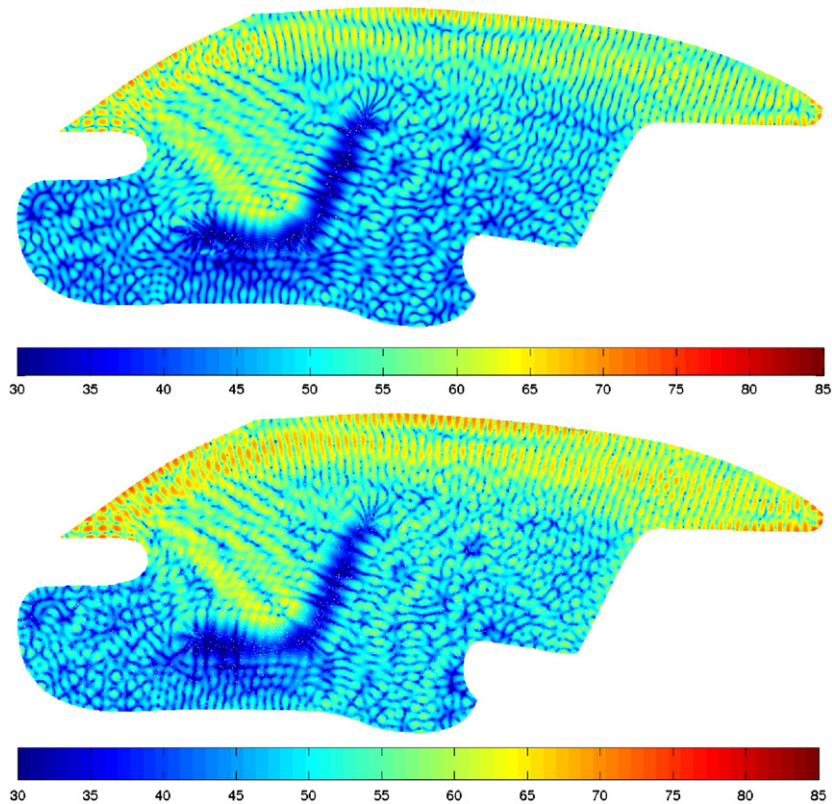


**Fig. 13.** Sound pressure field (in dB) with material D at 5000 Hz. PUFEM results computed with coarse mesh 1 (top) and standard FEM results (bottom).

interpolation using approximately 120 000 nodes. The results show a very good agreement and differences stem from graphical interpolation as evaluation points are not identical for both methods. Note that the comparison was not easy to realize due to mesh geometric distortions. Indeed a closer look at Fig. 11 reveals that the PUFEM mesh does not exactly

follow the original boundary (in blue color). This is because the coarse mesh was designed with quadratic interpolation functions. Consequently, the standard FEM mesh has been drawn so that it fits perfectly with the PUFEM coarse mesh.

In Fig. 14, we pushed the calculation to high frequency with  $f=10\,000$  Hz. The first figure (top) shows the sound pressure level distribution with material D. Few numerical tests were performed by taking different values for the parameter C until convergence was reached. In this case, it was found that  $C=25$  was sufficient. This yields  $N_{\text{dof}} = 16\,648$  giving  $n_\lambda \approx 2.65$ . The second figure (bottom) shows the sound pressure level distribution with material C. A quick glance at Fig. 15 reveals that, at 10 000 Hz, the imaginary part of the wavenumber is about four times higher than that of material D. With the coarse mesh 1, the parameter  $\kappa_p$  is too high ( $\exp(-\kappa_p) \approx 0.0001$ ) and the PUFEM cannot produce good solutions. To circumvent this difficulty, the coarse mesh 2 has been designed by refining the element mesh size in the porous domain. The parameter  $\kappa_p$  is now smaller and  $\exp(-\kappa_p) \approx 0.01$ . This allows to obtain converged solutions with  $C=20$ . The computation was performed with  $N_{\text{dof}} = 16\,117$  giving  $n_\lambda \approx 2.6$ . The gain is remarkable here as the use of conventional finite elements would require at least 15–20 times more variables to achieve the same accuracy. It is anticipated that a

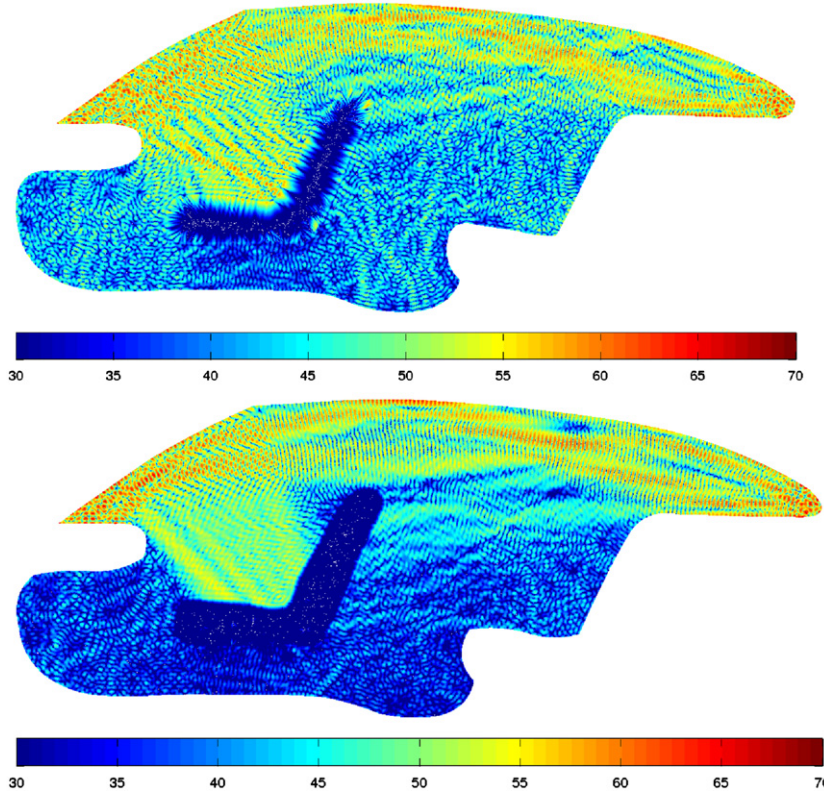


Fig. 14. Sound pressure field (in dB) at 10 000 Hz. PUFEM results computed with coarse mesh 1 with material D (top) and PUFEM results computed with coarse mesh 2 with material C (bottom).

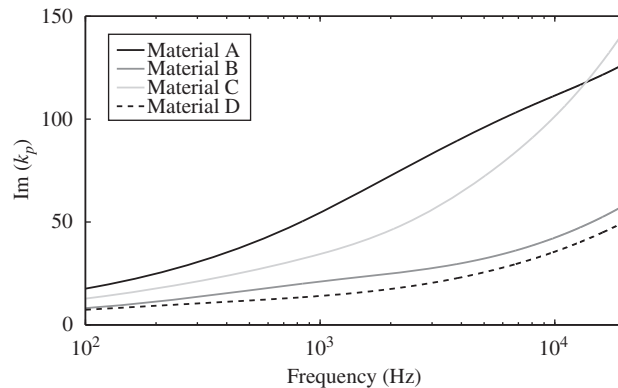


Fig. 15. Complex wavenumbers (imaginary part) for various materials.

similar analysis conducted in three dimensions would increase the gain by an additional factor of three to four [13].

**5. Conclusions**

This paper has demonstrated the applicability of the PUFEM for the numerical simulation of sound fields in two-dimensional cavities in which absorbing materials are present. These latter are modeled as a bulk-reacting material characterized by a complex-valued mean density and dynamic compressibility. The main ingredient of the method relies on the enrichment of the conventional finite element approximation by including a set of plane waves propagating in various directions. The performances of the method are assessed against a one-dimensional problem for which an analytical solution is available. It is concluded that best performances, measured in terms of data reduction, are obtained when the plane wave finite element spans over a large number of wavelengths. However, the imaginary part of the wavenumber of the pressure waves in the absorbing material may give rise to larger errors in the recombination of plane waves due to strongly evanescent waves and thus appears to be a limiting factor. Numerical applications presented in the Appendix of this paper show that the problem can be circumvented by refining adequately the mesh size in the porous domain. In this regard, we think that progress could be made by considering non-matching meshes at the air-porous interface. This would allow to keep large finite elements in the air domain regardless of the mesh size in the porous domain. In the mid-term, there is a need for a better geometric description of the domains' boundaries especially when the frequency increases. This could be done in the spirit of Deckers et al. [31] for instance. An efficient numerical or semi-analytical integration of element stiffness and mass matrices for curved elements should also be devised and we think there is a lot room for improvement in this direction. Finally, it is hoped that this work could serve as a starting point for the analysis of short wave problems involving poroelastic materials.

**Appendix A. Porous model**

The porous absorber is modeled as a rigid-frame material. The elastic and inertial contributions of the solid phase are therefore not taken into account. The remaining fluid phase is hence described as an equivalent fluid with viscous and thermal dissipations using the frequency-dependent Johnson–Champoux–Allard's expressions of the fluid density  $\rho_p$  and the dynamic fluid compressibility  $K_p$  [2]:

$$\rho_p = \rho_0 \alpha_\infty \left( 1 - \frac{\sigma \phi}{i \rho_0 \alpha_\infty \omega} \sqrt{1 - 4i \frac{\eta \alpha_\infty^2 \omega \rho_0}{\Lambda^2 \phi^2 \sigma^2}} \right), \tag{A.1}$$

$$K_p = \frac{\gamma P_0}{\gamma - (\gamma - 1) \left( 1 - \frac{8\eta \sqrt{1 - i \rho_0 \frac{Pr \Lambda'^2 \omega}{16\eta}}}{i \Lambda'^2 Pr \omega \rho_0} \right)^{-1}} \tag{A.2}$$

respectively, with  $i^2 = -1$ . These expressions are given with a time dependence in  $e^{-i\omega t}$ , and require also the knowledge of five semi-phenomenological parameters to efficiently take into account the pore geometry: the porosity  $\phi$ , the tortuosity  $\alpha_\infty$ , the airflow resistivity  $\sigma$ , and the viscous and thermal characteristic lengths  $\Lambda$  and  $\Lambda'$ . The characteristics of the surrounding fluid are given by its density  $\rho_0$ , its static pressure  $P_0$ , its dynamic viscosity  $\eta$ , its specific heat ratio  $\gamma$ , and the Prandtl number  $Pr$ . Figs. 15 and 16 show the value of the complex wavenumbers  $k_p = Re(k_p)(1 + i\chi)$  as function of the frequency for various materials denoted A–D. All other parameters such as the porosity, sound speed, density and so on

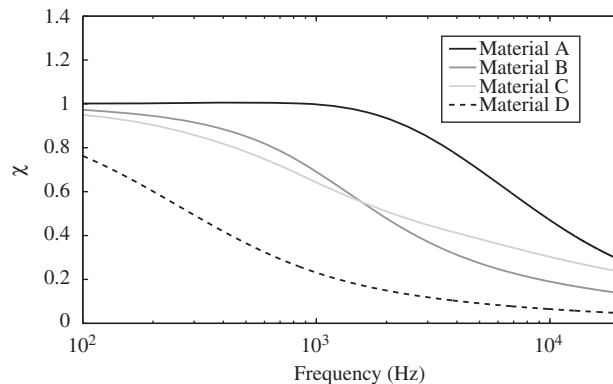


**Fig. 16.** Ratio between the imaginary and the real part of the wavenumber for various materials.

**Table A1**  
Characteristics of the materials.

Parameters	Mat A	Mat B	Mat C	Mat D
$\phi$	0.95	0.95	0.97	0.90
$\alpha_\infty$	1.00	1.00	1.54	7.8
$\sigma$ ( $10^3$ N m $^{-4}$ s)	105	23.0	57.0	25.0
$\Lambda$ ( $\mu$ m)	35.1	54.1	24.6	226
$\Lambda'$ ( $\mu$ m)	105.3	162.3	73.80	226
$\rho_s$ (kg m $^{-3}$ )	17	58	46	30

can be found in [28] for materials A–C. The material D refers to the FM2 foam in [29]. For the sake of completeness, the values are listed in Table A1.

## References

- [1] S. Marburg, B. Nolte, *Computational Acoustics of Noise Propagation in Fluids—Finite and Boundary Element Methods*, Springer-Verlag, Berlin, Heidelberg, 2008.
- [2] J.-F. Allard, N. Atalla, *Propagation of Sound in Porous Media: Modelling Sound Absorbing Materials*, John Wiley & Sons, 2009.
- [3] O. Dazel, N. Dauchez, The finite element method for porous materials, in: M. Bruneau, C. Potel (Eds.), *Materials and Acoustics Handbook*, John Wiley & Sons, 2009.
- [4] P. Bettess, Short wave scattering: problems and techniques, *Philosophical Transactions of the Royal Society of London A* 362 (2004) 421–443.
- [5] J.M. Melenk, I. Babuška, The partition of unity finite element method. Basic theory and applications, *Computer Methods in Applied Mechanics and Engineering* 139 (1996) 289–314.
- [6] O. Cessenat, B. Després, Application of an ultraweak variational formulation of elliptic PDEs to the two-dimensional Helmholtz problem, *SIAM Journal on Numerical Analysis* 35 (1998) 255–299.
- [7] T. Huttunen, P. Monk, J.P. Kaipio, Computational aspects of the ultra-weak variational formulation, *Journal of Computational Physics* 182 (2002) 27–46.
- [8] C. Farhat, I. Harari, U. Hetmaniuk, A discontinuous Galerkin method with plane waves and Lagrange multipliers for the solution of Helmholtz problems in the mid-frequency regime, *Computer Methods in Applied Mechanics and Engineering* 192 (2003) 1389–1419.
- [9] E. Perrey-Debain, J. Trevelyan, P. Bettess, Wave boundary elements: a theoretical overview presenting applications in scattering of short waves, *Engineering Analysis with Boundary Elements* 28 (2004) 131–141.
- [10] W. Desmet, P. Sas, D. Vandepitte, An indirect Trefftz method for the steady-state dynamic analysis of coupled vibro-acoustic systems, *Computer Assisted Mechanics and Engineering Sciences* 28 (2001) 271–288.
- [11] R. Lanoye, G. Vermeir, W. Lauriks, F. Sgard, W. Desmet, Prediction of the sound field above a patchwork of absorbing materials, *Journal of Acoustical Society of America* 123 (2008) 793–802.
- [12] H. Riou, P. Ladevèze, B. Sourcis, The multiscale VTGR approach applied to acoustics problems, *Journal of Computational Acoustics* 16 (2008) 487–505.
- [13] E. Perrey-Debain, O. Laghrouche, P. Bettess, J. Trevelyan, Plane wave basis finite elements and boundary elements for three dimensional wave scattering, *Philosophical Transactions of the Royal Society of London A* 362 (2004) 561–577.
- [14] M.S. Mohamed, O. Laghrouche, A. El-Kacimi, Some numerical aspects of the PUFEM for efficient solution of 2D Helmholtz problems, *Computers and Structures* 88 (2010) 1484–1491.
- [15] O. Laghrouche, M.S. Mohamed, Locally enriched finite elements for the Helmholtz equation in two dimensions, *Computers and Structures* 88 (2010) 1469–1473.
- [16] O. Laghrouche, P. Bettess, E. Perrey-Debain, J. Trevelyan, Wave interpolation finite elements for Helmholtz problems with jumps in the wave speed, *Computer Methods in Applied Mechanics and Engineering* 194 (2005) 367–381.
- [17] T. Stroubolis, R. Hidayat, I. Babuška, The generalized finite element method for Helmholtz equation. Part II. Effect of choice of handbook functions, error due to absorbing boundary conditions and its assessment, *Computer Methods in Applied Mechanics and Engineering* 197 (2007) 364–380.
- [18] T. Huttunen, P. Gamallo, R.J. Astley, Comparison of two wave element methods for the Helmholtz problem, *Communications in Numerical Methods in Engineering* 25 (2009) 35–52.
- [19] C. Geuzaine, J.-F. Remacle, Gmsh: a three-dimensional finite element mesh generator with built-in pre- and post-processing facilities, *International Journal for Numerical Methods in Engineering* 79 (2009) 1309–1331.
- [20] P. Bettess, J. Shirron, O. Laghrouche, B. Peseux, R. Sugimoto, J. Trevelyan, A numerical integration scheme for special finite elements for Helmholtz equation, *International Journal for Numerical Methods in Engineering* 56 (2003) 531–552.
- [21] G. Gabard, Exact integration of polynomial-exponential products with application to wave-based numerical methods, *Communications in Numerical Methods in Engineering* 25 (2009) 237–246.
- [22] A. El-Kacimi, O. Laghrouche, Improvement of PUFEM for the numerical solution of high-frequency elastic wave scattering on unstructured triangular mesh grids, *International Journal for Numerical Methods in Engineering* 84 (2010) 330–350.
- [23] W.H. Press, A.A. Teukolsky, W.T. Vetterling, B.P. Flannery, *Numerical Recipes in Fortran*, Cambridge University Press, Cambridge, 1992.
- [24] A. Moiola, R. Hiptmair, I. Perugia, Plane wave approximation of homogeneous Helmholtz solutions, *Zeitschrift für Angewandte Mathematik und Physik* 62 (2011) 809–837.
- [25] E. Perrey-Debain, Plane wave decomposition in the unit disc: convergence estimates and computational aspects, *Journal of Computational and Applied Mathematics* 193 (2006) 140–156.
- [26] H. Bériot, E. Perrey-Debain, M. Ben Tahar, C. Vayssade, Plane wave basis in Galerkin BEM for bidimensional wave scattering, *Engineering Analysis with Boundary Elements* 34 (2010) 130–143.
- [27] B. Nennig, E. Perrey-Debain, M. Ben Tahar, A mode matching method for modelling dissipative silencers lined with porous elastic materials and containing mean flow, *Journal of Acoustical Society of America* 128 (2010) 3308–3320.
- [28] O. Doutres, N. Dauchez, J.-M. Gènevaux, O. Dazel, Validity of the limp model for porous materials: a criterion based on the Biot theory, *Journal of Acoustical Society of America* 122 (2007) 2038–2048.
- [29] S. Rigobert, N. Atalla, F.C. Sgard, Investigation of the convergence of the mixed displacement pressure formulation for three-dimensional poroelastic materials using hierarchical elements, *Journal of Acoustical Society of America* 114 (2003) 2607–2617.
- [30] A.H. Barnett, T. Betcke, An exponentially convergent nonpolynomial finite element method for time-harmonic scattering from polygons, *SIAM Journal of Scientific Computing* 32 (2010) 1417–1441.
- [31] E. Deckers, B. Drofman, B. Van Genechten, B. Bergen, D. Vandepitte, W. Desmet, Spline-based boundaries: a first step towards generic geometric domain descriptions for efficient mid-frequency acoustic analysis using the wave based method, *Journal of Computational and Applied Mathematics* 235 (2011) 2679–2693.